small
NANO MICRO

Nanoparticles

Observation of Self-Assembled Core–Shell Structures in Epitaxially Embedded TbErAs Nanoparticles

*Pernell Dongmo, Matthew Hartshorne, Thomas Cristiani, Michael L. Jablonski, Cory Bomberger, Dieter Isheim, David N. Seidman, Mitra L. Taheri, and Joshua Zide**

Self-assembled core–shell structured rare-earth nanoparticles (TbErAs) are observed in a III–V semiconductor host matrix ($In_{0.53}Ga_{0.47}As$) nominally lattice-matched to InP, grown via molecular beam epitaxy. Atom probe tomography demonstrates that the TbErAs nanoparticles have a core–shell structure, as seen both in the tomographic atom-by-atom reconstruction and concentration profiles. A simple thermodynamic model is created to determine when it is energetically favorable to have core–shell structures; the results strongly agree with the observations.

1. Introduction

It has been shown that III-V semiconductor films containing rare-earth-based nanoparticles (e.g. ErAs, TbAs) can be beneficial for applications such as thermoelectrics, multi-junction solar cells, and terahertz sources/detectors. For thermoelectrics, incorporating ErAs or TbAs nanoparticles into lattice-matched InGaAs can reduce the thermal conductivity (compared to Si doped InGaAs) because of the increased phonon scattering.[1,2] Since these semimetallic nanoparticles act as dopants,[3] the mobility and conductivity of the films remain relatively high. In tunnel junctions, an increase in tunneling current can be seen when ErAs nanoparticles are embedded at the interface of the junction because of the formation of midgap states,[4] resulting in a more efficient tunnel junction. For terahertz materials, incorporating ErAs into GaAs has been shown to decrease carrier lifetimes and increase dark resistance (compared to low-temperature grown GaAs and radiation-damaged silicon-on-sapphire) because of the increased carrier recombination rates and pinning of the Fermi level.[5,6]

The properties of ErAs/TbAs in a III-V matrix have been studied for a number of years. It has been shown that ErAs or TbAs co-deposited with GaAs or InGaAs forms self-assembled, semimetallic nanoparticles with a rock-salt structure.[2,7–9] (**Figure 1**) shows the expected cross-sectional view for (a) mixed ErAs/TbAs core and (b) same mixed core with a TbAs shell. Because of the similar atomic numbers between Er and Tb, high angle annular dark field scanning transmission electron microscopy (HAADF-STEM) is insufficient to determine if the nanoparticle is a mixed core or a mixed core with a Tb shell. Atom probe tomography (APT), however, offers sufficient sub-nanoscale spatial and analytical resolution to clarify this issue.

As previously mentioned ErAs in GaAs has been extensively studied for terahertz applications. Currently, the industry standard materials are low-temperature (LT) grown GaAs (LT-GaAs), which provides fast carrier trapping time

P. Dongmo, C. Bomberger, Prof. J. Zide
Department of Materials Science and Engineering
University of Delaware
201 Dupont Hall, Newark, Delaware 19716, USA
E-mail: zide@udel.edu
T. Cristiani
Department of Chemical Engineering
University of Delaware
201 Dupont Hall, Newark, Delaware 19716, USA
M. Hartshorne, M. L. Jablonski, Prof. M. L. Taheri
Department of Materials Science and Engineering
Drexel University
LeBow Hall 441, Philadelphia, Pennsylvania 19104, USA
Prof. D. Isheim, Prof. D. N. Seidman
Department of Materials Science and Engineering
and Northwestern University Center for Atom-Probe Tomography
Northwestern University
2220 Campus Drive, Evanston, IL 60208–3108, USA

DOI: 10.1002/smll.201400891

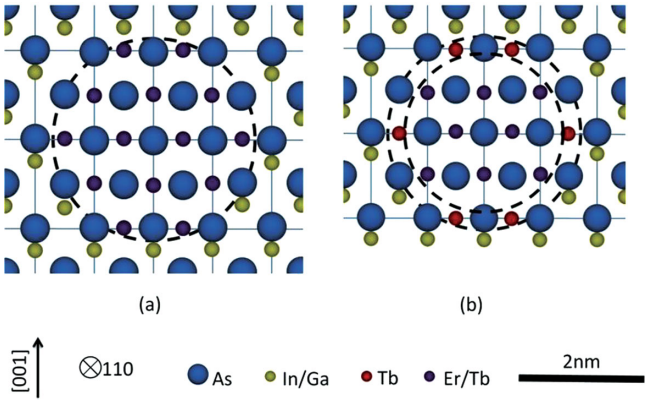

Figure 1. A cross-sectional view of (a) a mixed core of Er/Tb atoms and (b) a mixed core of Er/Tb atoms and a shell of Tb atoms. Each nanoparticle has a rock-salt crystal structure. Notice that In/Ga atoms appear everywhere except inside the nanoparticle, which is expected.

needed for terahertz generation and detection. However, LT-GaAs films have two major drawbacks: the response time and dark resistance are both controlled by growth and annealing temperature and cannot be independently tuned. These properties can be greatly affected by subsequent processing steps. Additionally, GaAs-based materials are only useful for photon energies greater then ~1.42 eV (the bandgap of GaAs), which prevents the use of these materials for excitation with 1.55 μm wavelength photons. 1.55 μm is desirable because it is the primary wavelength for fiber optic technologies,[10] and THz measurements can be performed with an inexpensive and compact 1.55 μm laser system rather than the typical 800 nm Ti:Sapphire laser system, which is significantly more expensive and difficult to operate.[11] O'Hara et al. studied the effects of ErAs nanoparticles in GaAs and showed that the response time and dark resistance can be independently tuned. Additionally, the ErAs nanoparticles provide a short carrier lifetime and the ErAs nanoparticles in GaAs showed much better performance than traditional LT-GaAs. Despite these advances, ErAs nanoparticles in GaAs nanoparticles can still not be pumped at 1.55 μm.[5] In an attempt to obtain a terahertz material capable of pumping at 1.55 μm, ErAs nanoparticles in InGaAs latticed matched to InP were studied. It was found that these nanoparticles in InGaAs latticed matched to InP provide short carrier lifetimes without the need of a post growth annealing step;[12–14] however the Fermi level is pinned above the conduction band[15] where a Fermi level pinned below the conduction band is desired to achieve a high dark resistance.[16] When the nanoparticles are embedded, Fermi level pinning occurs because the nanoparticles have a large density of states and behave like buried Schottky barriers.[15,17] The lattice constant for ErAs is 5.74 Å[18] and 5.82 Å[9] for TbAs. Depending on the host matrix, the nanoparticles can either cause a tensile or compressive strain which is believed to move the Fermi level up or down, respectively, from a universal donor level.[2,9,13] Because of this, it was believed that TbAs nanoparticles in InGaAs latticed matched to InP would pin the Fermi level below the conduction band, providing a high dark resistance, while providing the short carrier lifetimes that ErAs nanoparticles provide. However, Vanderhoef et al recently found that TbAs nanoparticles may be saturable, and would thus not have the short carrier lifetimes (at adequate excitation intensity) needed for terahertz applications.[19]

Thus, we expected that if a core-shell nanoparticle made of ErAs-TbAs embedded in $In_{0.53}Ga_{0.47}As$ (latticed matched to InP) was created, the TbAs shell could pin the Fermi level below the conduction band, resulting in a high dark resistance, and the ErAs core could provide the short carrier lifetimes needed for terahertz detection and generation. When both Er and Tb are co-deposited to either InGaAs or GaAs, we believed a core-shell nanoparticle would form through a strain-driven process. In this Letter, we demonstrate the crystal structure and composition of nanocomposite particles in which both terbium and erbium are incorporated into InGaAs (nominally lattice-matched to InP). Specifically, we demonstrate the apparent formation of core-shell nanostructures by APT and HAADF-STEM and a simple thermodynamic model that supports this observation.

2. Results and Discussion

An APT reconstruction of one of the ErAs/TbAs nanoparticles is shown in (**Figure 2**(a)) with the aid of isoconcentration surfaces delineating areas with Tb or Er concentrations higher than 5 at.%, respectively. The Tb isosurface, displayed in red, has a larger volume and completely encloses the Er isosurface, displayed in blue, demonstrating the core-shell structure of the NP with a TbAs shell and a mixed TbErAs core. (Figure 2(b)) displays the entire APT reconstruction volume with 5 at.% isoconcentration surfaces for Er and Tb, outlining many NP with an Er- rich core (blue surface) surrounded by a Tb-rich shell (red surfaces). (Figure 2(c)) is a proxigram concentration profile[20] graphing concentration with respect to distance, in three dimensions, from the 5 at.% Er isoconcentration surfaces shown in (Figure 2), which defines the origin of the profile. The proxigram profile demonstrates that the Tb enrichment extends much further out (negative distance values) from the Er-rich core of the NPs, at the right-hand side of the profile, with the core-shell interface being close to the origin represented by the 5 at.% Er isoconcentration surface. The grey line in (Figure 2(c)) is the Tb/Er concentration ratio, which has a maximum in the Tb-rich shell of the NPs.

Finally, a STEM-HAADF image of the ErAs/TbAs nanoparticle is shown in (**Figure 3**(a)), and a schematic of the STEM image can be seen in (Figure 3(b)). The particle appears coherent inside the InGaAs matrix with a measured diameter of 2.4 nm. In comparing the STEM-HAADF image to the schematic shown in Figure 1, the STEM-HAADF shows a presence of In/Ga atoms inside of the nanoparticle. This is due to the technique used to acquire the image; because electrons are transmitted through the film and the nanoparticles are embedded within the film, the electron beam will "see" both the Er/Tb atoms and the In/Ga atoms above and below the particle. As expected, it is not possible to differentiate which atom is Er/Tb or pure Tb using HAADF because of the similarities of their elastic scattering cross sections. Therefore, this technique alone is not adequate

small 2014,
DOI: 10.1002/smll.201400891

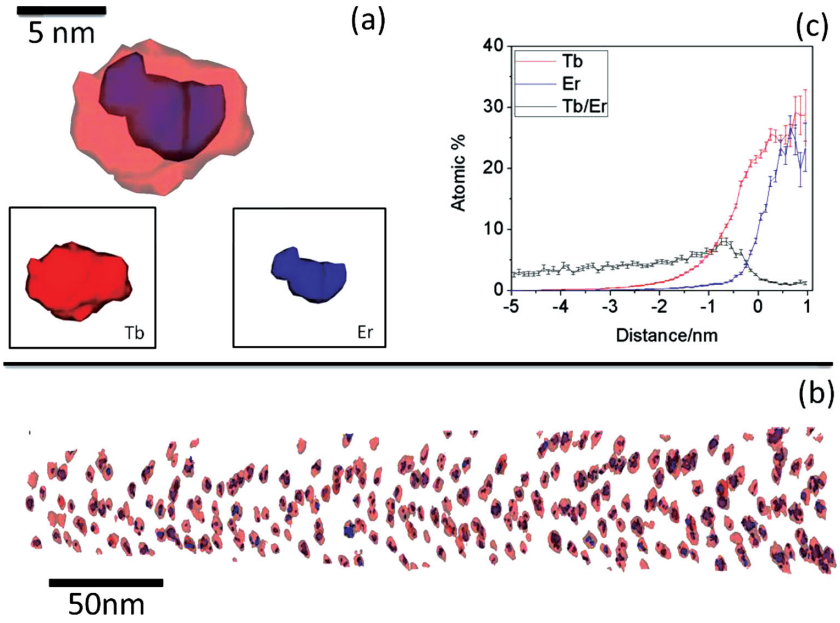

Figure 2. (a) An APT reconstruction of one of the nanoparticles with a 5 at.% terbium isoconcentration surface shown in red and a 5 at.% erbium isosurface shown in blue. The Er isosurface is completely contained inside of the Tb isosurface, suggesting a core-shell structured nanoparticle. (b) Isoconcentration surface analysis of the entire APT reconstruction volume showing the nanoparticles with 5 at.% Tb isosurfaces in red and 5 at.% Er isosurfaces in blue. Note that all Er-rich regions are surrounded by Tb-rich areas, but not all Tb-rich zones contain an Er enrichment. (c) Proxigram concentration profile with respect to the 5 at.% Er isoconcentration surfaces shown in Figure 2(b), with Er shown in blue, Tb shown in red and the Tb/Er concentration ratio in black, illustrating the maximum Tb/Er ratio in the Tb-rich shell.

enough to determine what type of nanoparticle is observed. It can, however, be correlated with the APT data to more accurately determine both composition of the particles.

The diameter of the nanoparticle observed in the STEM image in (Figure 3(a)) disagrees with the thickness of the particles shown in the isosurfaces in (Figure 2(a)). The apparent diameter of the particles in the x and y directions is approximately 6 nm; the diameter in the z direction is approximately 4 nm. The difference in diameter measured is likely caused by a combination of surface migration of atoms due to the increased temperature of the tip from the laser pulse[21] and local magnification effects.[22] The resurgence of pulsed laser atom probe has allowed for the analysis of semiconductors, but presents its own challenges. The stimulus for evaporation in conventional atom probe is the transient voltage pulse while the temperature is held constant. Pulsed laser atom probe holds the evaporation field constant, while using a thermal pulse from a laser to provide the energy required for evaporation. However, the thermal pulse in the presence of the standing field can also activate surface displacement mechanisms such as surface diffusion,[23–25] surface reconstruction[26] or migration of atoms from a high-coordination site to an adjacent low-coordination site.[27] Local magnification effects result from the local topography of the sample, which can be effected by the difference in evaporation potential of different phases.[22,28] The broadening of precipitates due to this

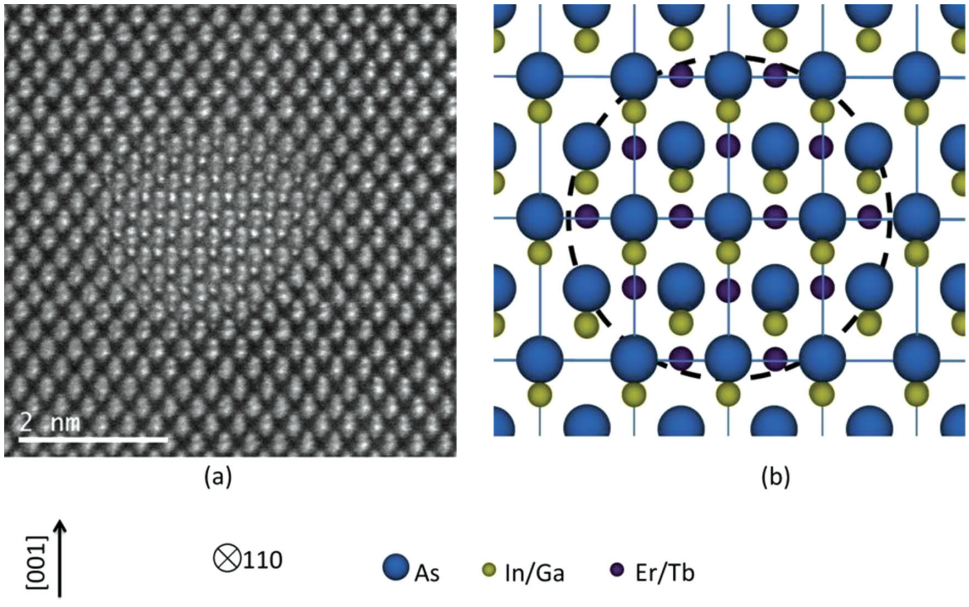

Figure 3. (a) Cs-corrected STEM-HAADF image of TbErAs nanoparticle inside the InGaAs film and (b) a schematic of the STEM-HAADF image. The diameter was measured to be 2.4 nm correlating to the approximated thickness from APT. In/Ga atoms appear "inside" of the nanoparticle because of the technique used to acquire the image. Because of similar Z-contrasts between Er and Tb, it is difficult to determine if the nanoparticle is a mixed core or a mixed core with a Tb shell.

DOI: 10.1002/smll.201400891

local magnification is consistent with a higher evaporation field for particles[29] of TbErAs than for InGaAs.

Resistivity and Hall measurements were also performed in the van der Pauw geometry at room temperature. The carrier concentration for the TbErAs:InGaAs material was 6.2×10^{17} cm^{-3}, which is lower than 0.3% ErAs:InGaAs (~2×10^{18} cm^{-3}),[30] as predicted. Unexpectedly, it is also lower than the carrier concentration of 0.78% TbAs:InGaAs (1.5×10^{18} cm^{-3}),[2] which warrants further investigation. The TbErAs:InGaAs film therefore has a higher resistivity ($4*10^{-3}$ Ω*cm) than 0.78% TbAs:InGaAs (1.2×10^{-3} Ω*cm),[2] which is favorable for terahertz materials as mentioned previously. The mobility of the film remained reasonably high (2497 cm^2/Vs), which is comparable to TbAs:InGaAs (3494 cm^2/Vs)[2] and ErAs:InGaAs (~3200 cm^2/Vs).[30] The slight reduction in mobility can be attributed to a relatively large nanoparticle concentration as described in section 4 below.

2.1. Thermodynamic Model

To explain the formation of a TbAs shell in these nanoparticles, a simple thermodynamic model was created to examine the energetics of the system. This model will determine what type of nanoparticles is likely to form in a material system that is not in thermodynamic equilibrium, but is in a metastable or kinetically-limited state. In this model, nine assumptions were made: (1) nanoparticles were considered spherical, (2) only configurational entropy and interfacial strain were calculated, (3) Young's modulus (E_{YM}) of ErAs and TbAs are assumed to be on the order of E_{YM} of GaAs, (4) the average E_{YM} and average lattice constant for a NP scale linearly with composition, (5) the growth temperature was 535 °C, (6) all NP shells are 99.9 at.% pure TbAs, and (7) the calculation considers both fractional atoms and fractional cation sites when computationally necessary. Because of the small lattice mismatch between the film and substrate, (8) volume strain energies were not included in the model. Since the bonding configuration for ErAs and TbAs are the same in a mixed nanoparticle and core-shell nanoparticle, (9) total bonding energies were not included in the calculations. For a given nanoparticle (NP), the overall free energy can be calculated using the relationship:

$$A = \pi r^2 \tag{1}$$

where H is the Helmholtz free energy, U is the internal energy (in this case, comprised of only interfacial bond strain), T is the absolute temperature in Kelvin, and S is the entropy. The configurational entropy of any core or shell region is found by using the expression:

$$S = k_B \ln \Omega \tag{2}$$

where k_B is Boltzmann's constant, and Ω is the total number of individual configurations of the region given by:

$$\Omega = \frac{A!}{(A+B)!\cdot B!} \tag{3}$$

where A is the total number of sites of component A in the region (ErAs) and B is the total number of sites of component B in the region (TbAs). For any core-shell NP, there are two regions of interfacial strain – at the core-shell interface and at the shell-substrate interface. The strain at each of these locations is found using the same method, which is derived from Hooke's Law. For an interface between regions 1 and 2, the interfacial strain is represented by:

$$E_{strain,interface} = N_{unit\ cells,\ interface} \cdot \frac{1}{2} \Delta \alpha_{interface}^{\ 2} \left[\left(E_{YM,avg,1} \cdot \alpha_{avg,1} \right) + \left(E_{YM,avg,2} \cdot \alpha_{avg,2} \right) \right] \tag{4}$$

$$N_{unit cells,interface} = SA_{interface} \cdot \frac{1}{2} \left(\frac{1}{a_{avg,1}^2} + \frac{1}{a_{avg,2}^2} \right) \tag{5}$$

where $N_{unit\ cells,\ interface}$ is the number of unit cell surfaces at the interface between two regions, $SA_{interface}$ is the interfacial surface area, $E_{YM,avg,I}$ is the average Young's modulus for a given region (obtained by a compositional average), $\Delta a_{interface}$ is the difference of average lattice constants at the interface, and $a_{avg,I}$ is the average lattice constant of a given region. Since there are no experimentally determined values for the Young's Moduli of pure ErAs and TbAs, we assumed it was the same order of magnitude as GaAs. Also, a weighted average was used to calculate the average value of E_{YM} and lattice constant. A plot of the free energy calculation can be seen in (**Figure 4**). The top curve represents a "pure" ErAs core/"pure" TbAs shell nanoparticle, the middle curve represents a mixed nanoparticle, and the bottom curve represents a mixed core with a "pure" TbAs shell. The model suggests

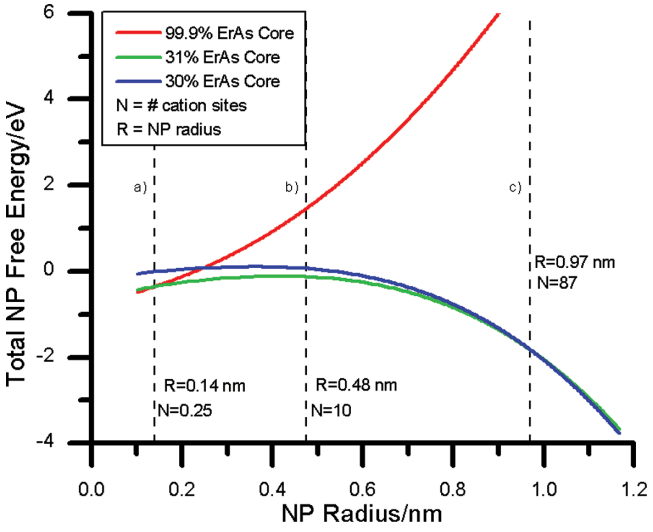

Figure 4. Free energy (FE) calculation of spherical $Tb_{0.7}Er_{0.3}As$ NPs in an InGaAs substrate with varying degrees of core-shell character plotted against the overall NP radius at a growth temperature of 535 °C. The red and green curves were calculated assuming a 99.9 atom% TbAs pure shell. The red curve represents a pure ErAs core/pure TbAs shell structure, the blue curve represents a mixed core and a mixed shell (or a mixed nanoparticle), and the green curve represents a mixed core with a thin TbAs pure shell. 99.9 atom% was used instead of 100 atom% because it is not experimentally possible to have 100 atom% TbAs shell or ErAs core. The missing 0.1% accounts for entropy. Thin-shell configuration is favorable between a) and c) while b) shows a "minimum" practical NP size.

small 2014,
DOI: 10.1002/smll.201400891

that it is practically impossible to have a "pure" ErAs core; the shell, however, is thermodynamically more favorable to be "pure" TbAs rather than mixed. It also shows that our nanoparticle diameter is at the limit where it is thermodynamically favorable to have a core-shell nanoparticle similar to what was observed. Although the material system is not in thermodynamic equilibrium, the system is in a metastable state. Since there is no kinetic driving force involved during deposition, the core-shell structure is formed under thermodynamically favorable conditions.

Even though it is thermodynamically favorable to have core-shell nanoparticles, all nanoparticles were not core-shell; some were pure TbAs nanoparticles. (Figure 2(c)) shows an APT reconstruction of the whole film. Every erbium-containing NP shown had a TbAs shell; however, not every TbAs NP had an Er-containing core. There are a couple of reasons why this occurred: (1) the film contained a higher concentration of Tb than Er, and (2) even though it is thermodynamically favorable to have core-shell, the difference in energy is small, and therefore there could be some fraction of TbAs nanoparticles that are in slightly-higher metastable states. Indeed, metastable structures are a hallmark of MBE growth.

3. Conclusion

We have demonstrated the growth of nanoparticles containing TbErAs incorporated into InGaAs. Both experimental evidence from APT and theoretical predictions strongly suggest these particles form self-assembled core-shell structures due to the effects of strain. These structures provide a new and useful method to tuning both the electronic properties of the particles and the interface with the semiconductor matrix.

4. Experimental Section

Sample Growth: The sample analyzed in this paper was grown via OSEMI NextGEN molecular beam epitaxy (MBE); the structure consisted of a 500 nm $In_{0.53}Ga_{0.47}As$ film (nominally lattice matched) co-deposited with erbium and terbium on a semi-insulating InP (100) substrate. The concentrations of Er and Tb were targeted to be 0.4% and 0.8% respectively. The film was grown under an arsenic overpressure of 1×10^{-5} torr with a growth temperature of 490 °C (measured by band edge thermometry). The film's growth rate was 0.28 μm/h. A streaky reflective high-energy electron diffraction (RHEED) pattern was observed during growth which indicated a smooth surface.

Atom Probe Tomography: Atom probe tomography (APT) was used to observe the structure of the nanoparticles in our sample. Data from APT experiments, which involves atom-by-atom analysis *via* laser pulsed ionization and mass spectrometry, can generate a 3D reconstruction of a specified area. A more detailed explanation can be found elsewhere.[31,32] The samples were prepared by a FEI DB235 FIB/SEM with an Omniprobe model 100.7 micromanipulator, placed on a standard SEM sample stub, and loaded onto a special liftout holder made by Fischione Instruments. This holder mounts both a standard specimen stub as well as six sample stubs for the Fischione model 2050 on-axis rotation tomography holder. A platinum capping layer was deposited using the electron beam, then reinforced with the ion beam depositing platinum. The samples were then individually lifted out onto tungsten stubs that had been sharpened by electropolishing in a two molar potassium hydroxide solution. Sharpening was accomplished by first annular milling the sample at 30 keV using first a 300 pA aperture followed by a 50 pA aperture to produce the requisite needle geometry. The sample was simultaneously formed and cleaned using a 5 keV defocused ion beam. The film and the substrate milled much faster than the Pt capping layer, which provided a sharp tip to the specimen as the platinum layer was eroded by the low keV ion beam. This process was monitored in SEM so that the milling could be stopped when only a very small amount of Pt remained. The sample was analyzed in a local-electrode atom probe (LEAP) 4000X-Si at Northwestern University. A 5 pJ laser pulse energy with a 250 kHz pulse repetition rate at 25 K base temperature was utilized during the analysis.

Imaging: A high angle annular dark field (HAADF) image of the sample was acquired by a probe-side spherical aberration corrected JEOL JEM-ARM200CF scanning transmission electron microscope (STEM). Preparation for the sample involved an initial thinning of the sample using a mechanical polish. A low speed polishing wheel was used with diamond lapping films to polish the material to sub-20 μm thickness. The samples were then thinned to electron transparency using low-angle ion mill operating at 5 kV with consecutively lower milling angles for each milling step.

Acknowledgements

MLT, MIH, and MLJ gratefully acknowledge support in part from the National Science Foundation under Early Career Award #1150807 and in part from the Office of Naval Research under grant #N00014–1101–0296. PBD, TRC, CCB, and JMOZ gratefully acknowledge funding from the National Science Foundation (DMR-1105137). We also acknowledge the National Science Foundation's MRSEC program (DMR-0520513) and made use of its Shared Facilities at the Materials Research Center of Northwestern University. The LEAP tomograph at NUCAPT was purchased and upgraded with funding from NSF-MRI (DMR-0420532) and ONR-DURIP (N00014–0400798, N00014–0610539, N00014–0910781) grants. Additional instrumentation at NUCAPT was supported by the Initiative for Sustainability and Energy at Northwestern.

[1] W. Kim, S. Singer, A. Majumdar, J. Zide, D. Klenov, *Nano Lett.* **2008**, 6–8.
[2] L. E. Clinger, G. Pernot, T. E. Buehl, P. G. Burke, A. C. Gossard, C. J. Palmstrøm, A. Shakouri, J. M. O. Zide, *J. Appl. Phys.* **2012**, *111*, 094312.
[3] D. C. Driscoll, M. Hanson, C. Kadow, A. C. Gossard, *Appl. Phys. Lett.* **2001**, *78*, 1703.
[4] J. M. O. Zide, A. Kleiman-Shwarsctein, N. C. Strandwitz, J. D. Zimmerman, T. Steenblock-Smith, A. C. Gossard, A. Forman, A. Ivanovskaya, G. D. Stucky, *Appl. Phys. Lett.* **2006**, *88*, 162103.

DOI: 10.1002/smll.201400891

[5] J. F. O'Hara, J. M. O. Zide, A. C. Gossard, A. J. Taylor, R. D. Averitt, *Appl. Phys. Lett.* **2006**, *88*, 251119.
[6] S. Sethi, P. K. Bhattacharya, *J. Electron. Mater.* **1996**, *25*, 467–477.
[7] D. O. Klenov, D. C. Driscoll, A. C. Gossard, S. Stemmer, *Appl. Phys. Lett.* **2005**, *86*, 111912.
[8] I. Poole, K. E. Singer, A. R. Peaker, A. C. Wright, *J. Cryst. Growth* **1992**, *121*, 121–131.
[9] L. E. Cassels, T. E. Buehl, P. G. Burke, C. J. Palmstrøm, A. C. Gossard, G. Pernot, A. Shakouri, C. R. Haughn, M. F. Doty, J. M. O. Zide, *J. Vac. Sci. Technol. B Microelectron. Nanom. Struct.* **2011**, *29*, 03C114.
[10] D. C. Driscoll, M. P. Hanson, A. C. Gossard, E. R. Brown, *Appl. Phys. Lett.* **2005**, *86*, 051908.
[11] M. Martin, J. Mangeney, P. Crozat, P. Mounaix, *Appl. Phys. Lett.* **2010**, *97*, 111112.
[12] C. Kadow, S. B. Fleischer, J. P. Ibbetson, J. E. Bowers, A. C. Gossard, J. W. Dong, C. J. Palmstrøm, *Appl. Phys. Lett.* **1999**, *75*, 3548.
[13] H.-T. Chen, W. J. Padilla, J. M. O. Zide, S. R. Bank, A. C. Gossard, A. J. Taylor, R. D. Averitt, *Opt. Lett.* **2007**, *32*, 1620.
[14] A. K. Azad, R. P. Prasankumar, D. Talbayev, A. J. Taylor, R. D. Averitt, J. M. O. Zide, H. Lu, A. C. Gossard, J. F. O'Hara, *Appl. Phys. Lett.* **2008**, *93*, 121108.
[15] J. M. O. Zide, J.-H. Bahk, R. Singh, M. Zebarjadi, G. Zeng, H. Lu, J. P. Feser, D. Xu, S. L. Singer, Z. X. Bian, A. Majumdar, J. E. Bowers, A. Shakouri, A. C. Gossard, *J. Appl. Phys.* **2010**, *108*, 123702.
[16] M. P. Hanson, S. R. Bank, J. M. O. Zide, J. D. Zimmerman, A. C. Gossard, *J. Cryst. Growth* **2007**, *301–302*, 4–9.
[17] K. Delaney, N. Spaldin, C. Van de Walle, *Phys. Rev. B* **2008**, *77*, 235117.
[18] S. Sethi, P. Bhattacharya, *J. Electron. Mater.* **1996**, *25*.
[19] L. R. Vanderhoef, A. K. Azad, C. C. Bomberger, D. R. Chowdhury, D. B. Chase, A. J. Taylor, J. M. O. Zide, M. F. Doty, *Phys. Rev. B* **2014**, *89*, 045418.
[20] O. Hellman, J. Vandenbroucke, J. Rüsing, D. Isheim, D. Seidman, *Microsc. Microanal.* **2000**, *6*, 437–444.
[21] B. Gault, M. Müller, A. La Fontaine, M. P. Moody, A. Shariq, A. Cerezo, S. P. Ringer, G. D. W. Smith, *J. Appl. Phys.* **2010**, *108*, 044904.
[22] M. K. Miller, M. K. Hetherington, *Surf. Sci.* **1991**, *246*, 442–449.
[23] C. G. Sánchez, A. Y. Lozovoi, A. Alavi, *Mol. Phys.* **2004**, *102*, 1045–1055.
[24] J. Neugebauer, M. Scheffler, *Surf. Sci. Lett.* **1993**, *287–288*, A404.
[25] L. Yao, B. Gault, J. M. Cairney, S. P. Ringer, *Philos. Mag. Lett.* **2010**, *90*, 121–129.
[26] A. J. Melmed, R. T. Tung, W. R. Graham, G. D. W. Smith, *Phys. Rev. Lett.* **1979**, *43*, 1521–1524.
[27] M. Wada, *J. Phys.* **1984**, *45*, 89–94.
[28] M. K. Miller, *J. Phys.* **1987**, *48*, 565–570.
[29] F. Vurpillot, A. Bostel, D. Blavette, *Appl. Phys. Lett.* **2000**, *76*, 3127.
[30] J. M. Zide, D. O. Klenov, S. Stemmer, A. C. Gossard, G. Zeng, J. E. Bowers, D. Vashaee, A. Shakouri, *Appl. Phys. Lett.* **2005**, *87*, 112102.
[31] T. F. Kelly, M. K. Miller, *Rev. Sci. Instrum.* **2007**, *78*, 031101.
[32] D. N. Seidman, *Annu. Rev. Mater. Res.* **2007**, *37*, 127–158.

Received: April 1, 2014
Revised: July 3, 2014
Published online:

DOI: 10.1002/smll.201400891